International Journal of Heat and Mass Transfer 141 (2019) 1301–1314

Contents lists available at ScienceDirect

International Journal of Heat and Mass Transfer

journal homepage: www.elsevier.com/locate/ijhmt

Analytical developments and experimental validation of a thermocouple model through an experimentally acquired impulse response function

J.I. Frankel *, Hongchu Chen

Department of Mechanical, Aerospace and Biomedical Engineering, University of Tennessee, Knoxville (UTK), TN 37996-2210, USA

ARTICLE INFO

Article history:
Received 6 April 2019
Received in revised form 18 May 2019
Accepted 28 May 2019
Available online 4 July 2019

Keywords:
Impulse response function
Experimental validation
Thermocouple modeling
Regularization
Volterra integral equation

ABSTRACT

This paper addresses the significance of and need for understanding the thermal impulse response function for (1) validating in-situ thermocouple models; and, (2) forming a "parameter free" inverse heat conduction methodology. The former application is the focus of the present study but it will be evident how to implement the findings of this presentation into the latter situation. The experimental component of this study utilizes a new small-sample, high-accuracy, electrical heating test facility for producing a quantifiable and accurate heat flux source. The impulse response kernel at the probe site is extracted and used for verifying the proposed in-depth thermocouple model. A linear, first-order thermocouple model is proposed based on the orientation of the probe and limited test temperature range. The location of the thermocouple and time constant are assumed known from some independent means or experiments. The impulse response function is determined and compared with the kernel of the resulting solution of the heat equation using the first-order model. Both kernels should nearly replicate if the model is not physically deficient. This preliminary investigation demonstrates a new means for (1) reconstructing the impulse response function and (2) validating a thermocouple model. Further, this experimentally generated impulse function can be used for resolving inverse heat conduction problems.

1. Introduction

High-quality and repeatable heat flux sources are in demand for calibration purposes that cover a large design space involving temperature, heating rate (°C/s), heat flux (W/m^2) and experimental run time. Three purposes for such a facility involve (1) the calibration of heat flux gauges [1–5]; (2) investigating and modeling in-depth thermocouples that correct for "smearing" [6–8] (i.e., relationship between measured thermocouple temperature and the required heat equation's positional temperature); and, (3) validating inverse heat conduction (IHC) methods. IHC formulations serve as a remote means for estimating the surface (net) heat flux or temperature [9–11]. Smearing implies attenuation and delay effects relative to the ideal signal as the sensor's response function is not of a true Dirac delta form [6–8].

Recently, a well-defined heat flux source has been demonstrated using an instrumented aluminum nitride substrate possessing a tungsten heater trace sandwiched between two in-depth resistance temperature detectors (RTD's). The entire heater is only 1.02 mm thick. Frankel et al. [12] describe the complete design to testing process that includes detailed model building and uncertainty analysis. In a nutshell, the heater is modeled and test cell property parameters are determined through a series of well-designed experiments guided by sensitivity analysis. This heater is used in a non-symmetric configuration that can produce a heat flux of 100 W/cm^2 possessing a temperature limit of approximately 400 °C. Owing to the initial design of the test cell, experimental run times are typically limited to less than 40 s. Through experimental validation studies, based on thin-slug calorimetry and model-based uncertainty analysis, the results indicate excellent accuracy for the design space [12]. The estimated total uncertainty for the departing one-sided heat flux is less than 5%.

2. Brief overview of experimental test facility (small sample heat flux cell)

Frankel et al. [12] describe the development of a new high-accuracy heat flux test cell. In that investigation, high repeatability was established as well as a high degree of accuracy for producing the exiting heat flux on the sample side. The first generation in-depth instrumented aluminum nitride (AlN) heater was designed with the following constraints $q'' < 100$ W/cm^2, $T < 400$ °C with a cross-sectional area of 6.45 cm^2 (1 sq. in.). This initial study was invoked for establishing a clear blueprint leading to an accurate sample-side heat flux characterization. The small sample test facility

* Corresponding author.
E-mail addresses: jfranke1@utk.edu (J.I. Frankel), hchen28@utk.edu (H. Chen).

https://doi.org/10.1016/j.ijheatmasstransfer.2019.05.098
0017-9310/

Nomenclature

A_s	cross-sectional surface area, 25.4 mm × 25.4 mm
b	probe position, m
$b_{nominal}$	nominal axial position of TC
c	specific heat, J/(kg K)
C	heat capacitance, J/K
$C_{\bar{\gamma}}$	constant, J/m^2
d_{hole}	thermocouple hole diameter, m
f	sampling frequency, Hz
k	thermal conductivity, W/(m K)
K	kernel function, Km^2/J
$\widehat{K}$	impulse response kernel, Km^2/J
$\widehat{K}_{\bar{\gamma}}$	approximate impulse response kernel, Km^2/J
$\widehat{K}_{\bar{\gamma}_{\bar{m}},\bar{N}}$	approximate impulse response kernel, Km^2/J
$\widetilde{\widehat{K}}_{\bar{\gamma}_{\bar{m}},\bar{N}}$	approximate impulse response kernel, Km^2/J
$\widetilde{\widehat{K}}_{\bar{\gamma}_{\bar{m},opt},\bar{N}}$	approximate impulse response kernel, Km^2/J
l	kernel function, s^{-1}
L	linear operator, (unitless)
M	functional operator, Km^2/J
$\bar{M}_f$	multiplication factor
$\bar{N}$	maximum number of data points
N_1	heat operator kernel function, m^{2}K/J
N_2	first-order TC model kernel, m^{2}K/J
P_j	model specific parameters
q''	heat flux, W/m^2
$\widetilde{q}''$	measured heat flux, W/m^2
R_K	cross correlation coefficient
$R_{\dot{K}}$	derivative cross correlation coefficient
t	time, s
t_{max}	maximum time for experiment, s
T	temperature, (K or °C)
T_0	temperature initial condition, (K or °C)
u	dummy time variable, s
V	voltage, V
V_o, V_1	voltage constants, V
x	spatial variable, m
z	dummy time variable, s

Greek symbols

α	thermal diffusivity, m^2/s
$\bar{\gamma}$	future-time parameter, s
$\bar{\gamma}_{\bar{m}}$	discrete spectrum of future-time parameters, s
$\bar{\gamma}_{\bar{m},opt}$	optimum future-time parameter, s
δ	dirac delta function
θ	reduced temperature, (K or °C)
$\widetilde{\theta}_{tc}$	reduced measured thermocouple temperature, (K or °C)
$\tilde{\theta}_{tc,\bar{\gamma}_{\bar{m},opt},\bar{N}}$	reconstructed reduced measured thermocouple temperature, (K or °C)
λ	coefficient, m^{2}K/(W s$^{1/2}$)
μ	dummy time variable, s
μ_o, μ_1	voltage function constants, s
ξ	time shifted variable, s
ρ	density, kg/m^3
σ_o, σ_1	voltage function constants, s
τ	thermocouple time constant, s

Subscripts

TF	thin-film thermocouple
TC	thermocouple
exp	experimental

is displayed in Fig. 1. A full characterization was performed on the heater and its surrounding insulation. The insulation used in the test cell is based on Zicar's Microsil™ whose thermal conductivity is approximately 0.025 W/m K in the defined temperature range.

3. Impulse kernel and mathematical formulation

As a preliminary investigation, the transient, one-dimensional linear heat equation described in a semi-infinite medium is used for illustrating principles and concepts. As this paper is motivated by its experimental outcomes, we begin by showing the experimental configuration, test cell and sample clamping prior to discussing the mathematical formulation. Fig. 2 displays the (a) physical test cell; (b) sample clamping; and, (c) schematic for mathematical model. The heater produces an excellent spatially uniform heating source for one-dimensional sample studies (under the appropriate 1-D, semi-infinite assumptions involving: temperature range, penetration times, two-dimensional edge effects, quality of the encapsulating insulation, etc.).

It should be recognized that the Non-Integer System Identification (NISI) method [13–18] is an inverse heat conduction method that is based on experimentally determining the impulse response function. This approach requires the determination of numerous experimentally derived system parameters based on a fractional derivative formulation and a least-squares procedure. Addressing the optimal number of parameters is somewhat problematic. This paper suggests an alternative methodology that only requires the determination of single parameter. In fact, the parameter being sought is the optimal regularization parameter. This paper offers a novel means for identifying the optimal regularization parameter which is the "crux" of all inverse problems.

This proposed semi-infinite analysis does not preclude generalization but permits visualization of the concepts in an easily understood geometrical framework. Therefore, the constant property heat equation, in the reduced temperature variable, $\theta(x,t) \triangleq T(x,t) - T_o$, is given as [19]

$$\frac{1}{\alpha}\frac{\partial \theta}{\partial t}(x,t) = \frac{\partial^2 \theta}{\partial x^2}(x,t), \quad x \in [0,\infty), \quad t \geqslant 0, \tag{1a}$$

subject to the boundary conditions

$$q''(0,t) = -k\frac{\partial \theta}{\partial x}(0,t), \qquad q''(\infty,t) = 0, \ (\text{or } \theta(\infty,t) = 0), \quad t \geqslant 0, \tag{1b, c}$$

and initial condition

$$\theta(x,0) = 0 \ , \quad x \in [0,\infty), \tag{1d}$$

where $T(x,t)$ is the temperature, T_o is the uniform initial condition, $q''(0,t)$ is the net surface heat flux, k is the thermal conductivity and α is the thermal diffusivity. The independent variables for space/time are denoted as x and t, respectively. For this study, the mathematical model side conditions are assumed adiabatic. The linear heat equation is valid for limited temperature ranges based on the material used. Note that the net surface heat flux, $q''(0,t)$ is experimentally provided as an outcome of the heater model described in Ref. [12] from the contact experiment. The equivalent integral form [20–22] of the differential system described in Eqs. (1a–d) is given as

$$\theta(x,t) = \int_{u=0}^{t} q''(0,u)K(x,t-u)du, \quad (x,t) \geqslant 0, \tag{2a}$$

where the kernel, $K(x,t-u)$ is given as

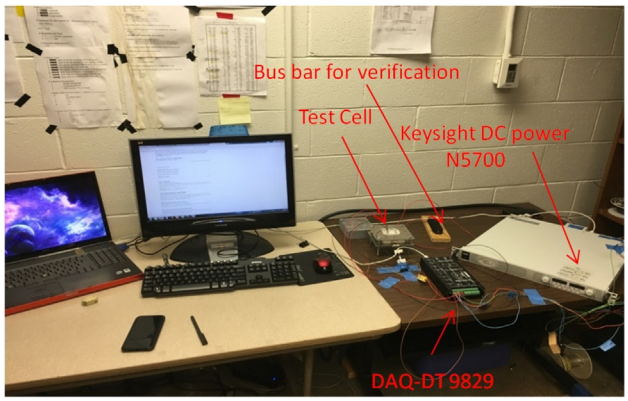

(a)

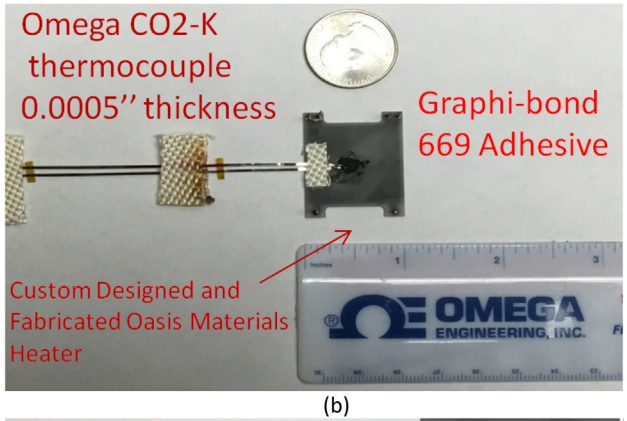

(b)

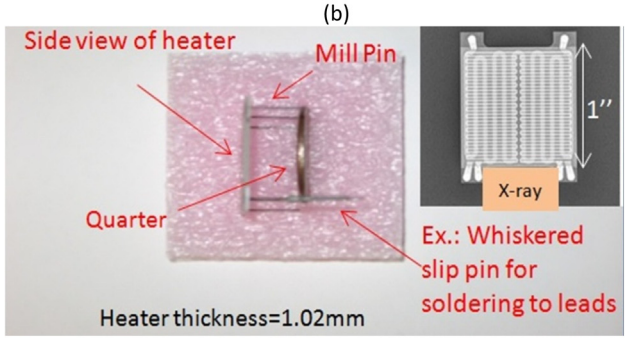

(c)

Fig. 1. a–c: Small sample test facility (a) overall set up, (b) heater geometry, and (c) heater x-ray.

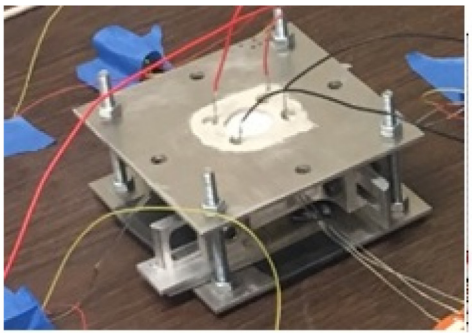

(a)

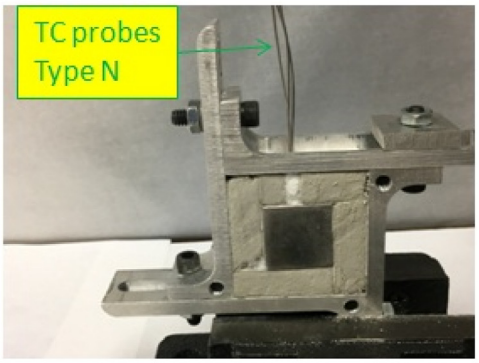

(b)

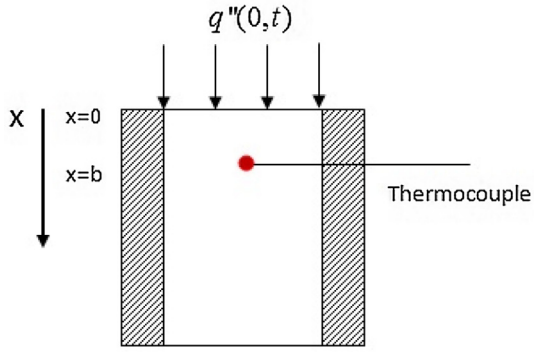

(c)

Fig. 2. Experimental configuration (a) physical test cell; (b) sampling clamping; and, (c) model schematic.

$$K(x,t-u)=\lambda\frac{e^{-\frac{x^2}{4\alpha(t-u)}}}{\sqrt{t-u}},\quad x>0,\quad t-u\geqslant 0\,, \tag{2b}$$

with the parameter $\lambda=\sqrt{\frac{\alpha}{\pi k^2}}=\frac{1}{\sqrt{\rho c k\pi}}$. This equivalence is demonstrated by the application of the Fourier cosine transforms (or Green's functions [23]). The convolution (or displacement) kernel given in Eq. (2b) is non-singular for $x>0$. Let us evaluate Eq. (2a) at $x=b>0$ to get

$$\theta(b,t)=\int_{u=0}^{t}q''(0,u)K(b,t-u)du,\quad t\geqslant 0\,. \tag{2c}$$

The reader is reminded that the reduced temperature, $\theta(b,t)$ is based on the positional temperature associated with the heat equation and not the probe/sensor temperature. That is, assuming that a thermocouple is located at $x=b>0$ suggests that $\theta(b,t)\neq\theta_{tc}(b,t)$. In-depth installed thermocouples, depending on whether it is an exposed bead, grounded or ungrounded encapsulation, produce various time constants based on its physical construction and chosen installation practices. Sheath orientation and other internal features can also play a role in establishing the positional temperature, $\theta(b,t)$. Further, conduction lead losses may occur. In order to relate the positional temperature to the measured temperature (basically removing the "smearing" effect, i.e., attenuation and delay), a model of the sensor is proposed as

$$L[\theta_{tc}(b,t)]=\theta(b,t),\quad t\geqslant 0, \tag{3a}$$

where L = linear functional operator that could be a differential or integro-differential operator. This operator, L will contain various "to be determined" properties (ex. in-situ time constant). For example, if an exposed thermocouple bead is placed at the in-depth position at $x=b>0$, and we assume that no conductive lead losses are present (say leads are parallel to isotherms though this does not assure a lack of lead losses) then a first-order model based

on a constant property energy balance performed about the exposed bead produces

$$\tau\frac{d\theta_{tc}}{dt}(b,t)+\theta_{tc}(b,t)=L[\theta_{tc}(b,t)]=\theta(b,t),\qquad t\geqslant 0, \tag{3b}$$

subject to $\theta_{tc}(b,0)=0$ as $\theta_{tc}(b,t)=T_{tc}(b,t)-T_o$ where τ is the so-called thermocouple time constant. Therefore, for this case, we identify L as

$$L=\tau\frac{d}{dt}+1. \tag{3c}$$

It is particularly revealing to express Eq. (2c) with Eq. (3a) substituted into the left-hand side. Performing this substitution and then inverting the operator L yields the symbolic form

$$\theta_{tc}(b,t)=L^{-1}(M[q'']),\quad t\geqslant 0, \tag{4a}$$

where M is the integral operator described by Eq. (2c). Explicitly expressing Eq. (4a) yields

$$\theta_{tc}(b,t)=\int_{z=0}^{t} l(t,z;\{P_j\}_{j=1}^{r})\int_{u=0}^{z} q''(0,u)K(b,z-u)dudz,\quad t\geqslant 0, \tag{4b}$$

where $\{P_j\}_{j=1}^{r}$ are the r-number of parameters in the thermocouple model, and $l(t,z;\{P_j\}_{j=1}^{r})$ is the inverted or resulting kernel function (ex. Green's function) associated with operator L. It is noted that the spatially evaluated kernel $K(b,z-u)$ possesses two thermophysical properties; namely, k and α. Changing orders of integration in Eq. (4b) on the defined triangle described by the limits of integration produces

$$\begin{aligned}\theta_{tc}(b,t)&=L^{-1}(M[q''])\\&=\int_{u=0}^{t} q''(0,u)\int_{z=u}^{t} l(t,z;\{P_j\}_{j=1}^{r})K(b,z-u)dzdu,\quad t\geqslant 0,\end{aligned} \tag{5a}$$

which can be expressed as

$$\theta_{tc}(b,t)=\int_{u=0}^{t} q''(0,u)\,\widehat{K}(t-u)du,\quad t\geqslant 0, \tag{5b}$$

where the new kernel function can be written as

$$\widehat{K}(t-u)=\int_{z=u}^{t} l(t,z;\{P_j\}_{j=1}^{r})K(b,z-u)dz,\quad t-u\geqslant 0. \tag{5c}$$

Observe that we have not explicitly defined the kernel function, $l(t,z;\{P_j\}_{j=1}^{r})$ but suggest its mere existence. As will be shown, the explicit form of this kernel is not necessary if a calibration process is pursued. An important observation arises if the surface heat flux could be represented by a Dirac delta function, that is, $q''(0,t)=\delta(t-0)$. Substituting this into Eq. (5b) produces the important result

$$\theta_{tc}(b,t)=\widehat{K}(t),\quad t\geqslant 0, \tag{5d}$$

which states that $\widehat{K}(t)$ is physically the in-depth thermocouple temperature response, $\theta_{tc}(b,t)$ to a surface impulse heat flux. The kernel $\widehat{K}(t)$ in reality is unknown due to several factors. However, this kernel function can be experimentally reconstructed if viewed as an inverse problem. That is, let us assume that a validated heat flux facility [12] is available and that a thermocouple is placed at $x=b>0$. The in-depth thermocouple installation will be assumed fixed among all future tests. For example, this can be checked by a mere electrical resistance measurement (when the TC is installed in an electrically conducting material). If the substrate is an electrical conductor then an Ohm meter can be used to measure the resistance between one thermocouple lead wire and the substrate. Once $\widehat{K}(t)$ is determined for fixed probe location then a thermocouple model can be compared with this experimentally arrived kernel that required no input parameters. Additionally, this kernel can be used for resolving the heat flux if postulated as an inverse heat conduction problem That is, this calibrated sensor-test article now accounts for the transducer's characteristics per Fig. 3. This paper focuses on developing the kernel function, $\widehat{K}(t)$ in a sound manner for future exploitation.

The rigorous formulation and systematic equation development described above are necessary ingredients for the detailed understanding of delays and attenuation effects introduced by an intrusive thermocouple (i.e., $T_{tc}(b,t)\neq T(b,t)$). Precision measurements require a validation procedure. The present study designs a means for experimentally validating a thermocouple model through the physically obtainable impulse response function.

4. Determining the impulse response kernel via calibration

Letting $\xi=t-u$ in Eq. (5b), and after some additional manipulations, produces

$$\theta_{tc}(b,t)=\int_{\xi=0}^{t}\widehat{K}(\xi)q''(0,t-\xi)d\xi,\quad t\geqslant 0, \tag{6}$$

where $q''(0,t-\xi)$ is now interpreted as the convolution kernel for the first-kind Volterra integral equation in the function $\widehat{K}(t)$ [20–22]. Further, as we are dealing with an experimental study, an upper time limit is now introduced as $t\in[0,t_{\max}]$ where $t_{\max}$ is the time where data are no longer collected. An experiment is proposed to determine the impulse response kernel, $\widehat{K}(t)$. The goal is now stated as "*Determine the impulse response kernel, $\widehat{K}(t)$ given measured inexact in-depth thermocouple data, $\theta_{tc}(b,t)$; and, given measured in-exact, net surface heat flux data, $q''(0,t)$ as produced from the heater model.*" Observe that the thermophysical and geometrical properties are not required in this statement. Further, only experimentally

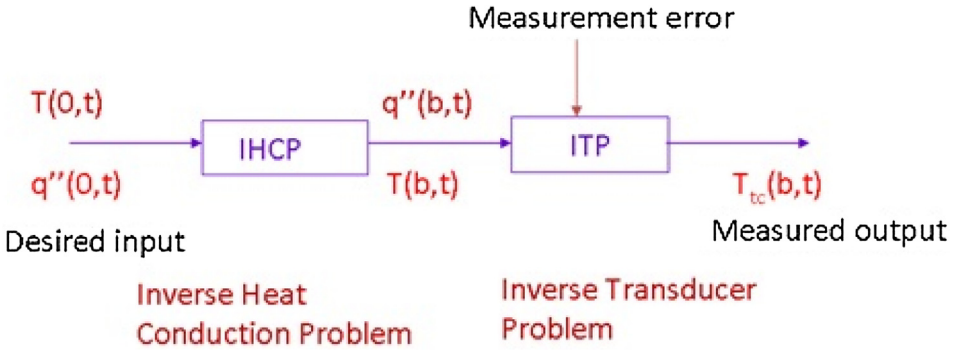

Fig. 3. Dissection of system/probe displaying inverse heat conduction problem (IHCP) and inverse transducer problem (ITP).

acquired data are used in the reconstruction of the impulse response kernel. Also note that the characterization of the thermocouple is built into the kernel $\widehat{K}(t)$ and hence not explicitly specified. That is, no transducer model (as suggested by Fig. 3) is proposed. However, results from this approach can be used for verifying a thermocouple transfer function model. Finally, the present formulation needs to be recast into a discrete setting for further analysis.

5. Inverse analysis by a future-time method

Starting with Eq. (6), let $t \to t + \bar{\gamma}$ thereby advancing time [24–26]. Doing so yields

$$\theta_{tc}(b, t+\bar{\gamma}) = \int_{\xi=0}^{t+\bar{\gamma}} \widehat{K}(\xi) q''(0, t+\bar{\gamma}-\xi) d\xi, \quad t \in [0, t_{\max}-\bar{\gamma}], \tag{7a}$$

which reduces the amount of recovery time for the impulse response kernel by $\bar{\gamma}$. Here, $\bar{\gamma}$ represents the future-time parameter, i.e., regularization parameter [9–11]. All inverse problems require regularization for stability to be recovered. The most difficult task lies in estimating the "optimal" regularization parameter. This initial study implements the future-time method for stabilization. This simple concept retains the causality feature and produces a simple computational procedure. Other methods, such as Singular-Value Decomposition (SVD) [27], are also available for stabilizing the numerical procedure. The SVD method does not retain causality. Eq. (7a) can be expressed as

$$\theta_{tc}(b, t+\bar{\gamma}) = \int_{\xi=0}^{t} \widehat{K}(\xi) q''(0, t+\bar{\gamma}-\xi) d\xi + \int_{\xi=t}^{t+\bar{\gamma}} \widehat{K}(\xi) q''(0, t+\bar{\gamma}-\xi) d\xi, \quad t \in [0, t_{\max}-\bar{\gamma}]. \tag{7b}$$

Assuming $\widehat{K}(\xi) \approx \widehat{K}(t)$ in the interval $\xi \in [t, t+\bar{\gamma}]$ for small $\bar{\gamma}$ produces the first approximation as

$$\theta_{tc}(b, t_i+\bar{\gamma}) \approx \int_{\xi=0}^{t} \widehat{K}(\xi) q''(0, t+\bar{\gamma}-\xi) d\xi + \widehat{K}(t) \int_{\xi=t}^{t+\bar{\gamma}} q''(0, t+\bar{\gamma}-\xi) d\xi, \quad t \in [0, t_{\max}-\bar{\gamma}]. \tag{7c}$$

In order to recover the equality, a change of notation is required; namely,

$$\theta_{tc}(b, t_i+\bar{\gamma}) = \int_{\xi=0}^{t} \widehat{K}_{\bar{\gamma}}(\xi) q''(0, t+\bar{\gamma}-\xi) d\xi + \widehat{K}_{\bar{\gamma}}(t) \int_{\xi=t}^{t+\bar{\gamma}} q''(0, t+\bar{\gamma}-\xi) d\xi, \ t \in [0, t_{\max}-\bar{\gamma}], \tag{7d}$$

where $\widehat{K}_{\bar{\gamma}}(t) \approx \widehat{K}(t)$. Next, if $\mu = t + \bar{\gamma} - \xi$ is substituted into the second integral in Eq. (7d) then Eq. (7d) can be written as

$$\theta_{tc}(b, t+\bar{\gamma}) = \int_{\xi=0}^{t} \widehat{K}_{\bar{\gamma}}(\xi) q''(0, t+\bar{\gamma}-\xi) d\xi + \widehat{K}_{\bar{\gamma}}(t) C_{\bar{\gamma}}, \ t \in [0, t_{\max}-\bar{\gamma}], \tag{7e}$$

where

$$C_{\bar{\gamma}} = \int_{\mu=0}^{\bar{\gamma}} q''(0, \mu) d\mu. \tag{7f}$$

Eq. (7e) is a second-kind Volterra integral equation [21] for $\widehat{K}_{\bar{\gamma}}(t)$. This mathematical structure possesses better stability characteristics for sufficiently large $C_{\bar{\gamma}}$ then the first-kind Volterra integral equation for $\widehat{K}(t)$ as displayed in Eq. (6). Next, form the discrete version of Eq. (7e) in preparation of using experimental data for both the in-depth temperature and net surface heat flux. Let $t \to t_i$, $i = 1, 2, ..., \bar{N} - \bar{m}\bar{M}_f$; and, therefore $\bar{\gamma} \to \bar{\gamma}_{\bar{m}} = \bar{m}\bar{M}_f \Delta t$, $\bar{m} = 1, 2, ..., \bar{M}$ where, $\bar{M}_f$ = convenient multiplication factor, $t_{\max} = \bar{N}\Delta t$ = total time of data collection, $\bar{N}$ = total number of sampled times beyond the initial condition; and, Δt = sampling time step. Evaluating Eq. (7e) at the discrete times produces

$$\theta_{tc}(b, t_i+\bar{\gamma}_{\bar{m}}) = \int_{\xi=0}^{t_i} \widehat{K}_{\bar{\gamma}_{\bar{m}}}(\xi) q''(0, t_i+\bar{\gamma}_{\bar{m}}-\xi) d\xi + \widehat{K}_{\bar{\gamma}_{\bar{m}}}(t_i) C_{\bar{\gamma}_{\bar{m}}}, \quad i = 1, 2, ..., \bar{N} - \bar{m}\bar{M}_f, \ \bar{m} = 1, 2, ..., \bar{M}, \tag{8a}$$

where

$$C_{\bar{\gamma}_{\bar{m}}} = \int_{\mu=0}^{\bar{\gamma}_{\bar{m}}} q''(0, \mu) d\mu, \quad \bar{m} = 1, 2, ..., \bar{M}. \tag{8b}$$

Fig. 4 aids visualizing the time-span reduction in resolving the impulse response kernel.

Eq. (8a) can alternately be expressed in the time segmented form (basic calculus)

$$\theta_{tc}(b, t_i+\bar{\gamma}_{\bar{m}}) = \sum_{j=1}^{i} \int_{\xi=t_{j-1}}^{t_j} \widehat{K}_{\bar{\gamma}_{\bar{m}}}(\xi) q''(0, t_i+\bar{\gamma}_{\bar{m}}-\xi) d\xi + \widehat{K}_{\bar{\gamma}_{\bar{m}}}(t_i) C_{\bar{\gamma}_{\bar{m}}}, \quad i = 1, 2, ..., \bar{N} - \bar{m}\bar{M}_f, \ \bar{m} = 1, 2, ..., \bar{M}. \tag{9a}$$

At this junction, a second approximation is now introduced based on discretizing Eq. (9a). A right-hand product integration rule is introduced into Eq. (9a) leading to [24–26]

$$\theta_{tc}(b, t_i+\bar{\gamma}_{\bar{m}}) \approx \sum_{j=1}^{i} \widehat{K}_{\bar{\gamma}_{\bar{m}}}(t_j) \int_{\xi=t_{j-1}}^{t_j} q''(0, t_i+\bar{\gamma}_{\bar{m}}-\xi) d\xi + \widehat{K}_{\bar{\gamma}_{\bar{m}}}(t_i) C_{\bar{\gamma}_{\bar{m}}}, \quad i = 1, 2, ..., \bar{N} - \bar{m}\bar{M}_f, \quad \bar{m} = 1, 2, ..., \bar{M}. \tag{9b}$$

In order to recover the equality, the approximation is denoted in the notation change given as

$$\theta_{tc}(b, t_i+\bar{\gamma}_{\bar{m}}) = \sum_{j=1}^{i} \widehat{K}_{\bar{\gamma}_{\bar{m}}, \bar{N}}(t_j) \int_{\xi=t_{j-1}}^{t_j} q''(0, t_i+\bar{\gamma}_{\bar{m}}-\xi) d\xi + \widehat{K}_{\bar{\gamma}_{\bar{m}}, \bar{N}}(t_i) C_{\bar{\gamma}_{\bar{m}}}, \quad i = 1, 2, ..., \bar{N} - \bar{m}\bar{M}_f, \quad \bar{m} = 1, 2, ..., \bar{M}, \tag{9c}$$

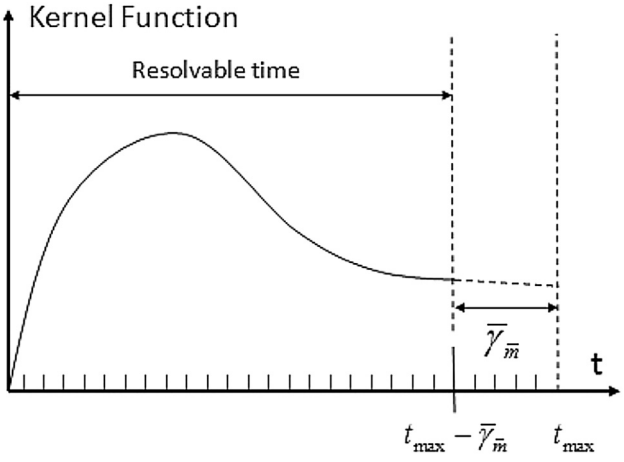

Fig. 4. Time reduction associated with the future-time method for resolving the impulse kernel problem.

where $\widehat{K}_{\bar{\gamma}_{\bar{m}},\bar{N}}(t_i) \approx \widehat{K}_{\bar{\gamma}_{\bar{m}}}(t_i) \approx \widehat{K}(t_i)$, $i = 1,2,...,\bar{N} - \bar{m}\bar{M}_f$, $\bar{m} = 1,2,...,\bar{M}$. A third approximation is now introduced into the estimation chain. An additional error is introduced into the approximation string associated with the collected temperature data, i.e., $\tilde{\theta}_{tc}(b,t_i) \approx \theta_{tc}(b,t_i)$, $i = 1,2,...,\bar{N} - \bar{m}\bar{M}_f$ and the "measured" net heat flux data denoted as $\tilde{q}''(0,t_i) \approx q''(0,t_i)$, $i = 1,2,...,\bar{N} - \bar{m}\bar{M}_f$. With these introductions into Eq. (9c), we obtain

$$\tilde{\theta}_{tc}(b,t_i + \bar{\gamma}_{\bar{m}}) \approx \sum_{j=1}^{i} \widehat{K}_{\bar{\gamma}_{\bar{m}},\bar{N}}(t_j) \int_{\xi=t_{j-1}}^{t_j} \tilde{q}''(0,t_i + \bar{\gamma}_{\bar{m}} - \xi)d\xi + \widehat{K}_{\bar{\gamma}_{\bar{m}},\bar{N}}(t_i) C_{\bar{\gamma}_{\bar{m}}},$$
$$i = 1,2,...,\bar{N} - \bar{m}\bar{M}_f, \quad \bar{m} = 1,2,...,\bar{M}. \tag{9d}$$

To recover the equality, Eq. (9d) is expressed as

$$\tilde{\theta}_{tc}(b,t_i + \bar{\gamma}_{\bar{m}}) = \sum_{j=1}^{i} \widetilde{\widehat{K}}_{\bar{\gamma}_{\bar{m}},\bar{N}}(t_j) \int_{\xi=t_{j-1}}^{t_j} \tilde{q}''(0,t_i + \bar{\gamma}_{\bar{m}} - \xi)d\xi + \widetilde{\widehat{K}}_{\bar{\gamma}_{\bar{m}},\bar{N}}(t_i) C_{\bar{\gamma}_{\bar{m}}},$$
$$i = 1,2,...,\bar{N} - \bar{m}\bar{M}_f, \ \bar{m} = 1,2,...,\bar{M}, \tag{9e}$$

where $\widetilde{\widehat{K}}_{\bar{\gamma}_{\bar{m}},\bar{N}}(t_i) \approx \widehat{K}_{\bar{\gamma}_{\bar{m}},\bar{N}}(t_i) \approx \widehat{K}_{\bar{\gamma}_{\bar{m}}}(t_i) \approx \widehat{K}(t_i)$, $i = 1,2,...,\bar{N} - \bar{m}\bar{M}_f$, $\bar{m} = 1,2,...,\bar{M}$. To recap, four approximations or assumptions have been introduced into this one-dimensional linear model. The first approximation is associated with stabilizing the ill-posed first kind Volterra integral equation (i.e., recasting into an approximate second kind integral equation for the unknown impulse response kernel). The second approximation is associated with the numerical discretization of the resulting integral equation. The third and fourth approximations are based on the introduction of experimental errors. The sampling frequency sets the time discretization, Δt^{-1}. The most difficult part in resolving inverse problems lies in the determination of the optimal regularization parameter. For this study, choosing the best or "optimal" future-time parameter, $\bar{\gamma}_{\bar{m},opt}$ is required from the discrete spectrum $\left\{\bar{\gamma}_{\bar{m}}\right\}_{\bar{m}=1}^{\bar{M}}$. Next, Eq. (9e) can be expressed in a time-marching form. To begin, release $j = i$ in the series on the right-hand side and perform operations that provide an explicit expression for $\widetilde{\widehat{K}}_{\bar{\gamma}_{\bar{m}},\bar{N}}(t_i)$. Doing so yields

$$\widetilde{\widehat{K}}_{\bar{\gamma}_{\bar{m}},\bar{N}}(t_i) = \frac{\tilde{\theta}_{tc}(b,t_i + \bar{\gamma}_{\bar{m}}) - \sum_{j=1}^{i-1} \widetilde{\widehat{K}}_{\bar{\gamma}_{\bar{m}},\bar{N}}(t_j) \int_{\xi=t_{j-1}}^{t_j} \tilde{q}''(0,t_i + \bar{\gamma}_{\bar{m}} - \xi)du}{\int_{\xi=t_{i-1}}^{t_i} \tilde{q}''(0,t_i + \bar{\gamma}_{\bar{m}} - \xi)d\xi + C_{\bar{\gamma}_{\bar{m}}}},$$
$$i = 1,2,...,\bar{N} - \bar{m}\bar{M}_f, \ \bar{m} = 1,2,...,\bar{M}, \tag{10}$$

which depends on the discrete spectrum of regularization parameters given as $\{\bar{\gamma}_{\bar{m}}\}_{\bar{m}=1}^{\bar{M}}$. The above numerical implementation is carefully described so the reader can quickly emulate the methodology. It should be noted and observed that Eq. (10) is easily programmable.

It is interesting to note that the in-depth reduced temperature measurements can be constructed using

$$\tilde{\theta}_{tc,\bar{\gamma}_{\bar{m},opt},\bar{N}}(b,t_i) = \int_{u=0}^{t_i} \widetilde{\widehat{K}}_{\bar{\gamma}_{\bar{m},opt},\bar{N}}(t_i - u)\tilde{q}''(0,u)du,$$
$$i = 1,2,...,\bar{N} - \bar{m}_{opt}\bar{M}_f, \tag{11}$$

when provided $\{\tilde{q}''(0,t_i)\}_{i=0}^{\bar{N}-\bar{m}_{opt}\bar{M}_f}$, $\{\widetilde{\widehat{K}}_{\bar{\gamma}_{\bar{m},opt},\bar{N}}(t_i - u)\}_{i=0}^{\bar{N}-\bar{m}_{opt}\bar{M}_f}$ and the optimal regularization parameter, $\bar{\gamma}_{\bar{m},opt}$. It should be noted that $\min||\tilde{\theta}_{tc,\bar{\gamma}_{\bar{m}},\bar{N}}(b,t_i) - \tilde{\theta}_{tc}(b,t_i)||_2^2$, $\bar{m} = 1,2,...,\bar{M}$ may ***not*** suggest the correct optimal regularization parameter for the surface heat flux in an inverse heat conduction study. This is important to note and will shortly be illustrated. Additionally, this concept does not preclude developing different calibration data sets based on different frequencies.

6. Results for experimentally determining the "Best impulse response kernel

A large set of test conditions were examined based on the experimental system's limitations and design space. In a nutshell and to recap, the experimental test cell has a temperature limit of 400 °C, heat flux limit of 100 W/cm^2. A time span of less than approximately 30 s [12] is used for assuring the geometric assumptions previously outlined. As this is a linear model and initial study, the main limitation lies in the temperature range and time span. Hence, the heater's temperature for this investigation does not exceed approximately 200 °C. It can be stated that the thermocouples' (Type N probe, Type K thin film) lead data were investigated for validating a normal distribution in errors. Additionally, a similar spectral study was performed on the net surface heat flux yielding a similar normal distribution in the lead data.

The first part of the experimental investigation lies in reconstructing the impulse response kernel, $\widetilde{\widehat{K}}_{\bar{\gamma}_{\bar{m},opt},\bar{N}}(t_i - u)$ over the regularization spectrum. The experimental process for producing the surface heat flux to the sample is based on controlling the heater's voltage to generate the power in the heater. The heater's departing energy flow is carefully described and analyzed in Ref. [12]. Table 1 displays several test runs (in voltage) considered in the test plan matrix. The voltages and parameter sets described in Table 1 are provided to the heater through LabVIEW and defined by

$$V(t) = V_o e^{-\left(\frac{t-\mu_o}{\sigma_o}\right)^2}, \ t \geqslant 0, \tag{12}$$

and

$$V(t) = V_o e^{-\left(\frac{t-\mu_o}{\sigma_o}\right)^2} + V_1 e^{-\left(\frac{t-\mu_1}{\sigma_1}\right)^2}, \ t \geqslant 0. \tag{13}$$

These cases and others were extensively examined. For this paper, focus is directed to Case 1 (most stringent among Cases 1–3 and attempts to represent an impulse shape). The in-depth thermocouple probe is an Omega NMQXL-032E-6, Type N with exposed bead having a stainless steel sheath diameter of 0.813 mm. The drilled hole in the sample has a diameter of 0.9652 mm and is nominally located at 0.3175 mm from the active surface. This position will shortly be re-visited and examined. Fig. 5 displays the estimated net heat flux into the stainless steel sample.

Table 1
Matrix test plan and voltage.

Case number	Description
1	Single Gauss (f = 20 Hz, V_o = 138.56 Volt, μ_o = 5 s, σ_o = 0.5 s), Eq. (12)
2	Single Gauss (f = 20 Hz, V_o = 97.98 Volt, μ_o = 5 s, σ_o = 1.0 s), Eq. (12)
3	Single Gauss (f = 20 Hz, V_o = 80 Volt, μ_o = 5 s, σ_o = 1.5 s), Eq. (12)
4	Single Gauss (f = 53.3 Hz, V_o = 138.56 Volt, μ_o = 5 s, σ_o = 0.5 s), Eq. (12)
5	Double Gauss (f = 20 Hz, V_o = 130 Volt, μ_o = 3 s, σ_o = 1 s and V_1 = 110 Volt, μ_1 = 7 s, σ_1 = 1 s), Eq. (13)
6	Double Gauss (f = 53.3 Hz, V_o = 130 Volt, μ_o = 3 s, σ_o = 1 s and V_1 = 110 Volt, μ_1 = 7 s, σ_1 = 1 s), Eq. (13)

From Fig. 5, a heat flux peak of approximately 80 W/cm^2 is generated. An estimate for the surface temperature is available as the material properties are known per

$$\tilde{\theta}(0,t) = \tilde{T}(0,t) - T_o = \sqrt{\frac{\alpha}{\pi}}\frac{1}{k}\int_{u=0}^{t} q''_{\exp}(0,u)\frac{du}{\sqrt{t-u}}, \quad t \geqslant 0, \quad (14)$$

as thermal penetration to the back or side surfaces has yet not occurred. The semi-infinite heat conduction model is assumed valid. Using room temperature properties ($k = 14.7$ W/m K, $\rho = 7900$ kg/m^3, $c = 477$ J/kg K [28]), a simple product integration rule [22] provides the reduced surface temperature, $\tilde{\theta}(0,t)$ per Eq. (14). Fig. 6 shows the corresponding estimated reduced surface temperature. A 110 °C maximum temperature difference appears between the front and back surfaces of the sample. The linear model with properties evaluated at room temperature appears appropriate based on the temperature dependent properties of stainless steel 304 [28]. This was also numerically verified.

The reconstruction of the impulse response kernel is now considered using the in-depth thermocouple temperature, $\tilde{\theta}_{tc}(b,t_i)$ and estimated heat flux [12], $\tilde{q}''(0,t_i)$, $i = 1,2,\ldots,\bar{N}$. Eq. (10) is called upon for forming the impulse response kernel, $\tilde{\tilde{K}}_{\bar{\gamma}_{\bar{m}},\bar{N}}(t_i)$, $i = 1,2,\ldots,\bar{N}-\bar{m}\bar{M}_f$, $\bar{m} = 1,2,\ldots,\bar{M}$ over the future-time regularization spectrum, $\bar{\gamma}_{\bar{m}}$, $\bar{m} = 1,2,\ldots,\bar{M}$. For this study, $\bar{M} = 10$, $\bar{M}_f = 5$, $\bar{N} = 280$, $\bar{\gamma}_{\bar{m}} = \bar{m}\bar{M}_f\Delta t = \bar{m}\bar{M}_f/20$. Fig. 7a–d display the resulting kernels for Case 1 using a sampling frequency of 20 Hz.

Fig. 7a–d display both the stability issues associated with inverse problems and the reduction in time caused by the future-time method (end padding). It is evident from Fig. 7a that the computation of the impulse response kernel when $\bar{\gamma}_{\bar{m}=6} = 1.5$ s is unstable implying insufficient smoothing (retaining too many high frequencies in the signal). In contrast, Fig. 7d is extremely smooth in light of noisy data. This implies that the regularization parameter, $\bar{\gamma}_{\bar{m}=9} = 2.25$ s is most likely over-smoothing the prediction (not retaining enough high frequencies in the signal). However, one can quickly observe that the optimal regularization parameter, $\bar{\gamma}_{\bar{m},opt}$ lies between 1.75 and 2.25 s. The determination of this fundamental parameter is sought for definiteness of the system. As no convergence rules actually exist for ill-posed, discrete inverse problems, an alternative view is proposed based on the formation

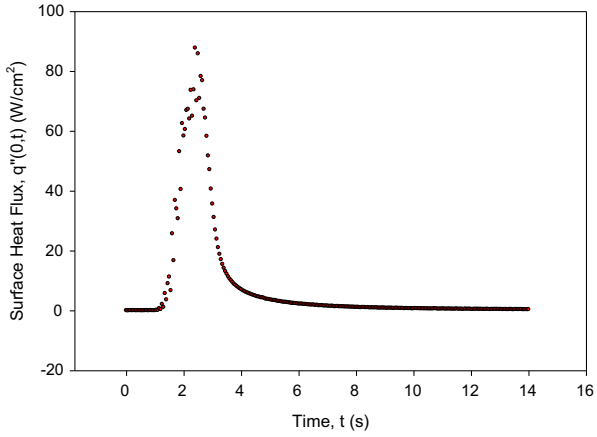

Fig. 5. Raw time history of surface (net) heat flux retaining some lead data as estimated by the procedure described in Ref. [12] for Case 1 described in Table 1 (t_{max} = 14 s, f = 20 Hz).

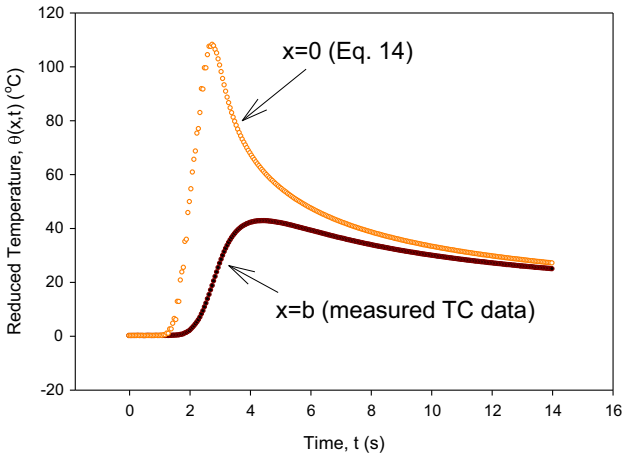

Fig. 6. Estimation of the sample's surface (positional) temperature and measured in-depth thermocouple (not positional) temperature.

of a pattern. With this said, it is important to realize that in all inverse problems, the error in the desired function decreases to some minimal value and then rises again as a function of regularization parameter. This is the hallmark of an ill-posed problem.

A physics based rule set is proposed based on understanding how information is propagated from the in-depth sensor to the surface. As all data are propagated through the linear heat operator, H given as $H \triangleq \frac{1}{\alpha}\frac{\partial}{\partial t} - \frac{\partial^2}{\partial x^2}$, this suggests that the controlling factor is associated with the time derivative (whether it is temperature or heat flux). The one-dimensional, constant property heat equation can be expressed in terms of temperature or heat flux and they both possess the identical heat operator, H. With that said, a physics based rule is suggested using the thermal phase plane and cross correlation. The thermal phase plane [24,25] is analogous to the mechanical/dynamic phase plane involving displacement and velocity where time is parameterized. The phase plane provides insightful qualitative behavior while cross correlation provides a quantitative metric.

As we seek the impulse response function, $\tilde{\tilde{K}}_{\bar{\gamma}_{\bar{m}},\bar{N}}(t_i)$, $i = 1,2,\ldots,\bar{N}-\bar{m}\bar{M}_f$, $\bar{m} = 1,2,\ldots,\bar{M}$ which is analogous to heat flux (when resolving the inverse heat conduction problem), the phase plane in this context should contain the time-rate of change of the impulse response kernel. Fig. 8a–d present the corresponding phase planes associated with Fig. 7a–d.

From Fig. 8a–d, a clear pattern in the parameterized space is occurring. Fig. 8a displays instability while Fig. 8c displays the onset of a pattern (compare Fig. 8c and d) and defines the "cusp" of stability. In fact, Fig. 8c displays the optimal value for the present conditions. Often, a single metric is desired by many researchers. For this work, a cross-correlation coefficient (normalized, i.e., ≤ 1) phase plane can be developed analogous to the previous phase plane. Cross correlation is also known as a sliding dot product [24] owing to it analogous behavior describing orthogonality of functions. The equations for the normalized cross-correlation coefficient are defined in Refs. [24,25] and given as

$$R_K(\tilde{\tilde{K}}_{\bar{\gamma}_{\bar{m}},\bar{N}}, \tilde{\tilde{K}}_{\bar{\gamma}_{\bar{m}+1},\bar{N}}) = \frac{\sum_{j=0}^{\bar{N}-(\bar{m}+1)\bar{M}_f} \tilde{\tilde{K}}_{\bar{\gamma}_{\bar{m}},\bar{N}}(t_j)\tilde{\tilde{K}}_{\bar{\gamma}_{\bar{m}+1},\bar{N}}(t_j)}{\sqrt{\sum_{j=0}^{\bar{N}-(\bar{m}+1)\bar{M}_f}\left(\tilde{\tilde{K}}_{\bar{\gamma}_{\bar{m}},\bar{N}}(t_j)\right)^2}\sqrt{\sum_{j=0}^{\bar{N}-(\bar{m}+1)\bar{M}_f}\left(\tilde{\tilde{K}}_{\bar{\gamma}_{\bar{m}+1},\bar{N}}(t_j)\right)^2}}, \quad (15a)$$

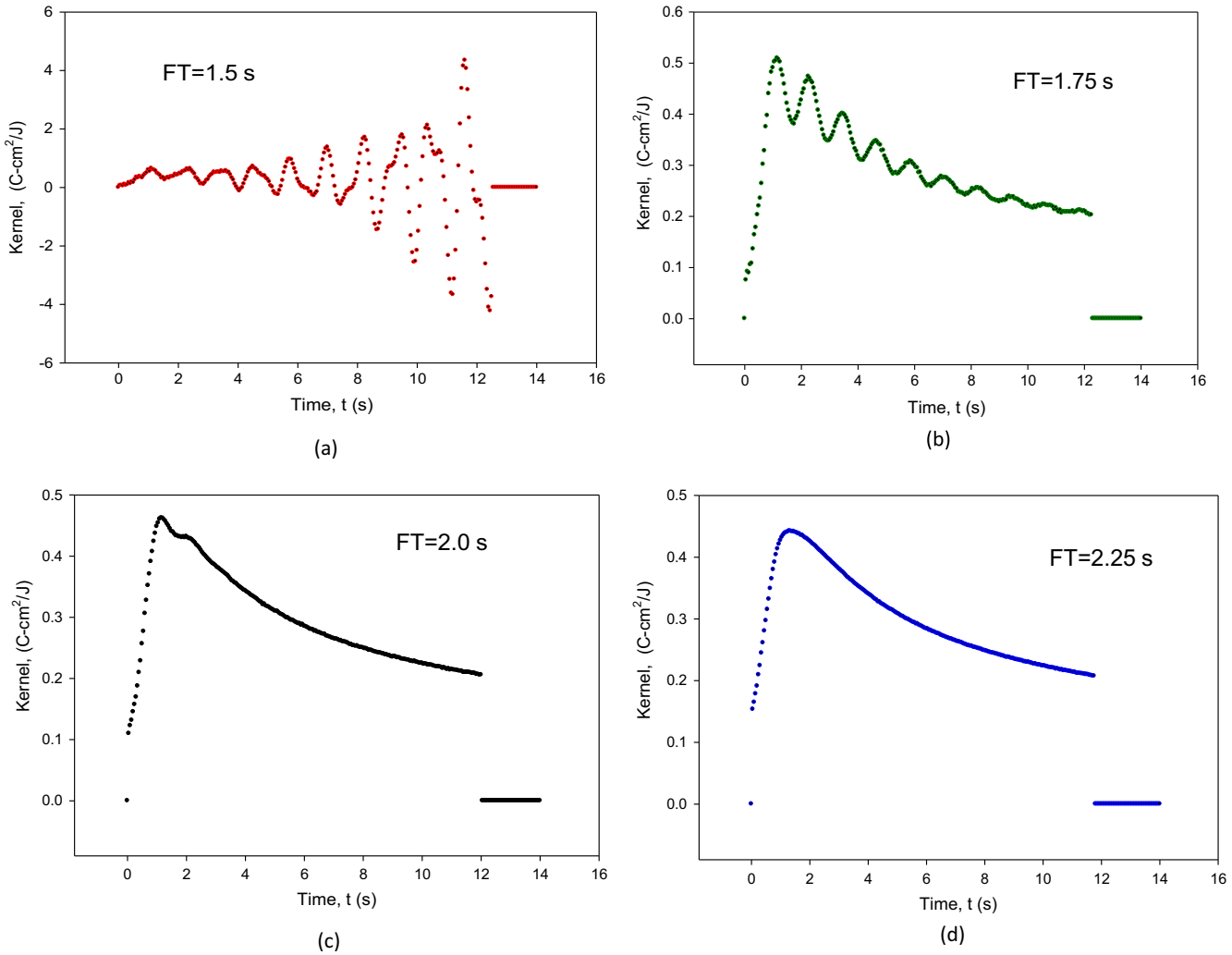

Fig. 7. Transient impulse response kernels, $\tilde{\tilde{K}}_{\bar{\gamma}_{\bar{m}},\bar{N}}(t_i)$, $i = 1,2,\ldots,\bar{N}-\bar{m}\,\bar{M}_f$, $\bar{m} = 6-9$ using various future-time (FT) parameters: (a) $\bar{\gamma}_{\bar{m}=6} = 1.5$ s; (b) $\bar{\gamma}_{\bar{m}=7} = 1.75$ s; (c) $\bar{\gamma}_{\bar{m}=8} = 2.0$ s; and, (d) $\bar{\gamma}_{\bar{m}=9} = 2.25$ s when the sampling frequency is 20 Hz.

and

$$R_K(\dot{\tilde{K}}_{\bar{\gamma}_{\bar{m}},\bar{N}}, \dot{\tilde{K}}_{\bar{\gamma}_{\bar{m}+1},\bar{N}}) = \frac{\sum_{j=0}^{\bar{N}-(\bar{m}+1)\bar{M}_f} \dot{\tilde{K}}_{\bar{\gamma}_{\bar{m}},\bar{N}}(t_j)\dot{\tilde{K}}_{\bar{\gamma}_{\bar{m}+1},\bar{N}}(t_j)}{\sqrt{\sum_{j=0}^{\bar{N}-(\bar{m}+1)\bar{M}_f}\left(\dot{\tilde{K}}_{\bar{\gamma}_{\bar{m}},\bar{N}}(t_j)\right)^2}\sqrt{\sum_{j=0}^{\bar{N}-(\bar{m}+1)\bar{M}_f}\left(\dot{\tilde{K}}_{\bar{\gamma}_{\bar{m}+1},\bar{N}}(t_j)\right)^2}}. \tag{15b}$$

For the present study, phase shifting is not included as its rational for omission is described in Ref. [25]. The phase-plane and cross correlation analyzes are presented to close the optimal approximation process. As such, the entire methodology is available for immediate implementation by the reader.

Fig. 9 and Table 2 contain detailed metric information on both behavior and quantification. Fig. 9 displays the resulting impulse response kernel cross-correlation phase plane (time derivatives are estimated using central difference approximations for interior points; and, simple forward and backward for the end points). The data sequences correlate as the cross-correlation coefficient approaches unity. A zero implies uncorrelated (orthogonal). Fig. 9 shows that the cross-correlation coefficient for $R_K(\tilde{\tilde{K}}_{\bar{\gamma}_{\bar{m}},\bar{N}}, \tilde{\tilde{K}}_{\bar{\gamma}_{\bar{m}+1},\bar{N}})$ approaches unity faster than $R_K(\dot{\tilde{K}}_{\bar{\gamma}_{\bar{m}},\bar{N}}, \dot{\tilde{K}}_{\bar{\gamma}_{\bar{m}+1},\bar{N}})$ approaching unity. Further, time derivatives of noisy (non-ideal) data should impede this movement toward unity. In fact, driving $R_K(\dot{\tilde{K}}_{\bar{\gamma}_{\bar{m}},\bar{N}}, \dot{\tilde{K}}_{\bar{\gamma}_{\bar{m}+1},\bar{N}})$ to unity makes little sense if any noise is present in the system. Table 2 further helps clarify the situation. Table 2 shows that $R_K(\dot{\tilde{K}}_{\bar{\gamma}_{\bar{m}},\bar{N}}, \dot{\tilde{K}}_{\bar{\gamma}_{\bar{m}+1},\bar{N}})$ is the key player for identifying the proper choice of the regularization parameter, $\bar{\gamma}_{\bar{m}}$. Table 2 strongly suggests that the instability-stability "cusp" occurs at $\bar{\gamma}_8 = 2$ s. A clear formation of a pattern begins as $(\bar{m},\ \bar{m}+1) \to (7,8)$ which describes the effect of smoothing as demonstrated through stability of the time derivative in the impulse response kernel. In this pairing, often the smaller $\bar{m}$ value is used to retain higher frequencies for heat flux [25]. However, reviewing the jump from the lower left side toward the upper right side; and, considering Figs. 7c, d and 8c, d suggest choosing $\bar{\gamma}_8 = 2$ s. Some art and science experience are required similar to digital filtering studies. Departure from drawn tangent line starting at the over-smoothed pairings shown in Fig. 9 provides a visual reference guide.

It was noted earlier (via Eq. (11)) that using the measured surface heat flux from the calibration source and the impulse response kernel, $\tilde{\tilde{K}}_{\bar{\gamma}_{\bar{m}},\bar{N}}(t)$ over the $\bar{\gamma}_{\bar{m}}$ spectrum does not assure the best estimate of the regularization parameter when reconstructing the in-depth temperature. This is partially indicated in

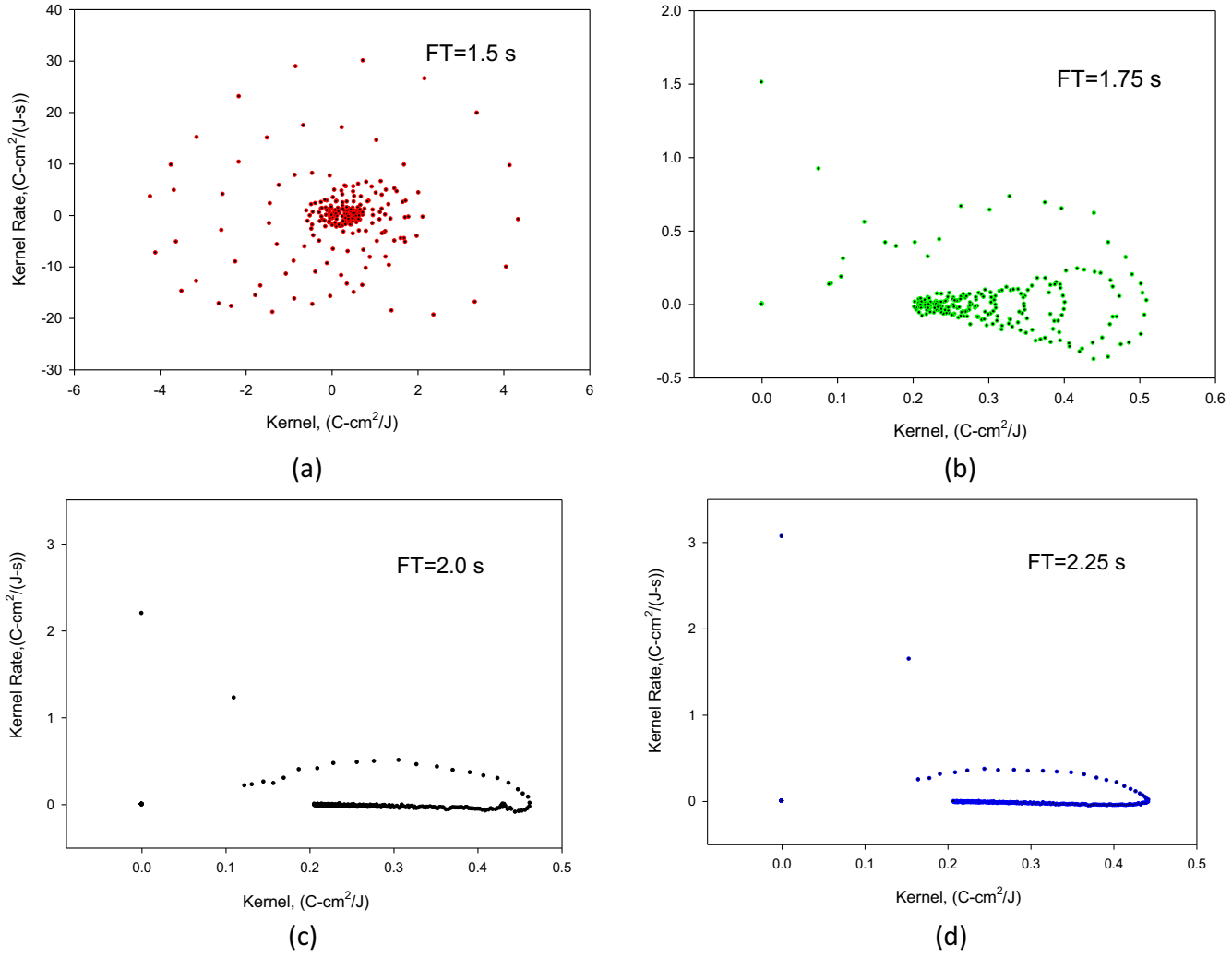

Fig. 8. Transient impulse response kernel phase plane using various future-time (**FT**) parameters: (a) $\bar{\gamma}_{\bar{m}=6} = 1.5\,\mathrm{s}$; (b) $\bar{\gamma}_{\bar{m}=7} = 1.75\,\mathrm{s}$; (c) $\bar{\gamma}_{\bar{m}=8} = 2.0\,\mathrm{s}$; and, (d) $\bar{\gamma}_{\bar{m}=9} = 2.25\,\mathrm{s}$ when the sampling frequency is 20 Hz.

Table 3. The root-mean square difference (RMSD) calculation suggests that the minimum occurs at $\bar{\gamma}_{\bar{m}=7} = \bar{\gamma}_{\bar{m},opt}$ which is incorrect (see Fig. 7b or Fig. 8b). The best regularization parameter should be developed based on the desired quantity of interest, i.e., $\widetilde{\bar{K}}_{\bar{\gamma}_{\bar{m}},\bar{N}}(t)$ and its corresponding time derivative (controlling factor). It is interesting to note that graphically $\bar{\gamma}_7$, $\bar{\gamma}_8$ produce similar reconstruction plots of the in-depth ($x = b$) temperature histories.

Before concluding this paper, let us revisit Case 1 but increase the sampling rate to 53.3 Hz (now Case 4 in Table 1). The surface heat flux estimated by the heater analysis is displayed in Fig. 10a while the estimated reduced surface temperature, via Eq. (14), and in-depth thermocouple reduced temperature are indicated in Fig. 10b.

Fig. 11 displays the resulting impulse response kernels using four different values of the regularization parameter, $\bar{\gamma}_{\bar{m}}$. A similar graphical sequencing to that of Fig. 7 is displayed. However, as sampling refinement is used, a smaller optimal regularization parameter is produced; namely, $\bar{\gamma}_{\bar{m},opt} = 1.5\,\mathrm{s}$ (note that $\Delta t = 1/53.3$ s).

Increasing the sampling frequency can impact the time differentiation operations. Fig. 12 presents the corresponding phase plane illustrating a similar feature to that of Fig. 8. From the qualitative information provided by Fig. 12, the optimal regularization parameter appears to be $\bar{\gamma}_{\bar{m},opt} = 1.5\,\mathrm{s}$. Following the previous discussion, the cross-correlation coefficient analysis confirms this value for the optimal future-time parameter as shown in Fig. 13. Finally, overlaying Fig. 7c onto Fig. 11c (not shown) indicates excellent agreement in the reconstruction of the impulse response function at the probe site.

A couple analytical observations are available placing perspective in the prediction of the experimental impulse response kernel using a non-perfect sensor. Recall that the present heat conduction problem can be recast as

$$T(x,t) - T_o = \sqrt{\frac{\alpha}{\pi}}\frac{1}{k}\int_{u=0}^{t} q''(0,u)\frac{e^{-\frac{x^2}{4\alpha(t-u)}}}{\sqrt{t-u}}du\,, \quad (x,t) \geqslant 0, \tag{16a}$$

and when evaluated at $x = b > 0$ produces

$$\theta(b,t) = T(b,t) - T_o = \sqrt{\frac{\alpha}{\pi}}\frac{1}{k}\int_{u=0}^{t} q''(0,u)\frac{e^{-\frac{b^2}{4\alpha(t-u)}}}{\sqrt{t-u}}du\,, \quad t \geqslant 0, \tag{16b}$$

or

$$\theta(b,t) = \int_{u=0}^{t} q''(0,u)N_1(b,t-u;k,\alpha)du\,, \quad t \geqslant 0, \tag{16c}$$

where

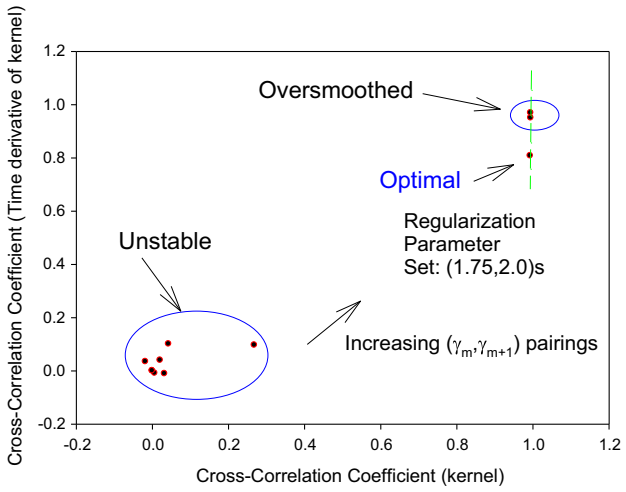

Fig. 9. Cross-correlation coefficient phase plane.

Table 2
Cross-correlation coefficients corresponding to Fig. 9.

$\bar{m}$, $\bar{m}+1$	$\bar{\gamma}_{\bar{m}}$, $\bar{\gamma}_{\bar{m}+1}$(s)	$R_K(\tilde{\tilde{K}}_{\bar{\gamma}_{\bar{m}},\bar{N}}, \tilde{\tilde{K}}_{\bar{\gamma}_{\bar{m}+1},\bar{N}})$	$R_K(\dot{\tilde{K}}_{\bar{\gamma}_{\bar{m}},\bar{N}}, \dot{\tilde{K}}_{\bar{\gamma}_{\bar{m}+1},\bar{N}})$
1,2	0.25, 0.5	0.0428	0.101
2,3	0.5, 0.75	0.0323	−0.0109
3,4	0.75, 1	0.0208	0.0395
4,5	1.0, 1.25	−0.0179	0.0341
5,6	1.25, 1.5	0.00663	−0.00913
6,7	1.5, 1.75	0.268	0.0961
7,8	1.75, 2.0	0.993	0.808
8,9	2.0, 2.25	0.995	0.950
9,10	2.25, 2.5	0.994	0.969

Table 3
Root-mean-square deviation (RMSD) of the in-depth temperature for Case 1.

$\bar{m}$	$\bar{\gamma}_{\bar{m}}$ (s)	Root mean square deviation (RMSD) (°C)
2	0.5	2.3×10^{63}
3	0.75	1.3×10^{74}
4	1.0	1.1×10^{55}
5	1.25	1.4×10^{19}
6	1.5	0.75
7	1.75	0.18
8	2.0	0.46
9	2.25	0.98
10	2.5	1.7

$$N_1(b,t-u;k,\alpha) \triangleq \sqrt{\frac{\alpha}{\pi}}\frac{1}{k}\frac{e^{-\frac{b^2}{4\alpha(t-u)}}}{\sqrt{t-u}},\ b \geqslant 0,\ \ t-u \geqslant 0. \tag{16d}$$

Eq. (16d) displays the ideal heat operator kernel or ideal impulse response kernel. Further, the experimental arrangement suggests that a first-order thermocouple model may be appropriate if the correct positioning, b and time constant, τ are known. The combined first-order model (control volume about the bead in the hole without consideration of conductive lead losses) yields

$$\tau\frac{d\theta_{tc}}{dt}(b,t)+\theta_{tc}(b,t)=\int_{u=0}^{t} q''(0,u)N_1(b,t-u;k,\alpha)du\,,\quad t \geqslant 0. \tag{17a}$$

If a calibration quality surface heat flux is known and in-depth thermocouple data are present then both τ, b can be estimated by a least-square method applied to Eq. (17a) when provided both k, α. Often the question arises "How good is the thermocouple model?". Another important application to this study involves answering this question. Case 3 in Table 1 is used to generate τ, b based on Eq. (17a). The time derivative term was discretized by central difference for interior points and forward/backward for time 0 and t_{max}, respectively. The thermophysical properties k, α were evaluated at room temperature (300 K). The least-squares result for these parameters are $\tau = 0.2$ s, $b = 2.77$ mm. The nominal value for the probe's axial position from the active side surface is $b_{nominal} = 3.175$ mm. The least-squares prediction produces a value that is within the nominal value of $b_{nominal} \pm \frac{d_{hole}}{2}$ where the hole diameter is 0.965 mm. Evaluating the properties at 100 °C and replicating the least square calculation produces similar estimates.

Using an integrating factor, and after a straightforward series of analytic manipulations, Eq. (17a) can be expressed in the fundamental form

$$\theta_{tc}(b,t)=\int_{u=0}^{t} q''(0,u)\,N_2(b,t-u;k,\alpha,\tau)du,\quad t \geqslant 0\,, \tag{17b}$$

where

$$N_2(b,t-u;k,\alpha,\tau) \triangleq \sqrt{\frac{\alpha}{\tau k^2}}\frac{e^{-\frac{t-u}{\tau}}}{2i}\left\{e^{-i\frac{b}{\sqrt{\alpha\tau}}}erfc\left(\frac{b/2}{\sqrt{\alpha(t-u)}}-i\sqrt{\frac{t-u}{\tau}}\right)-e^{i\frac{b}{\sqrt{\alpha\tau}}}erfc\left(\frac{b/2}{\sqrt{\alpha(t-u)}}+i\sqrt{\frac{t-u}{\tau}}\right)\right\}, \tag{17c}$$

which can be shown to be a real function (here, $i^2 = -1$). It should be noted that Eq. (17c) can directly be used to find τ, b in a least-squares sense.

Fig. 14a, b display the kernels for the (i) ideal thermocouple, N_1, Eq. (16d); (ii) first-order model, N_2, Eq. (17c); and, (iii) reconstructed kernel, $\tilde{\tilde{K}}_{\bar{\gamma}_{\bar{m}},\bar{N}}$, Eq. (10). Again, Case 1 is presented owing to its physical voltage input (and resulting heat flux) severity at the 20 Hz sampling. Several observations are now noted. Recall that the phase plane (Fig. 9) and cross-correlation coefficient (Table 2) previously suggested $\bar{\gamma}_8 = 2\,\text{s} = \bar{\gamma}_{\bar{m},opt}$. Notice that this prediction aligns well with the first-order thermocouple model kernel, N_2. This closeness to N_2 suggests that assuming the time constant to be zero is not well informed. The early-time wave in the reconstruction can be partial due to measured heat flux (see Fig. 5. between 1 and 3 s) and/or other physical effects occurring in the probe itself. Further, it suggest that classical inverse heat conduction ("parameter required") methods should consider the effect of the transducer as it does introduce a secondary inverse problem associated with the intrusiveness of the probe and installation procedure. For this investigation, the cross check suggests that the thermocouple model has merit and the time constant of $\tau = 0.2$ s is highly reasonable based on our experimental experiences and previous tests.

7. Conclusions

The primary contribution of this study involved establishing a rigorous methodology for validating a thermocouple model through the impulse response function as generated in a calibrated heat flux test cell. To demonstrate this, a sample was prepared where the thermocouple probe was installed parallel to the isotherm to minimize conductive lead losses in the probe. A thermocouple model is proposed and the parameters are experimentally estimated via a parameter estimation method. By comparing the impulse response function, which is based on the physical condition of the probe-sample assembly, the thermocouple model can be validated and provide confidence in the modeling process. Further, the positional temperature is recovered. It is well known that

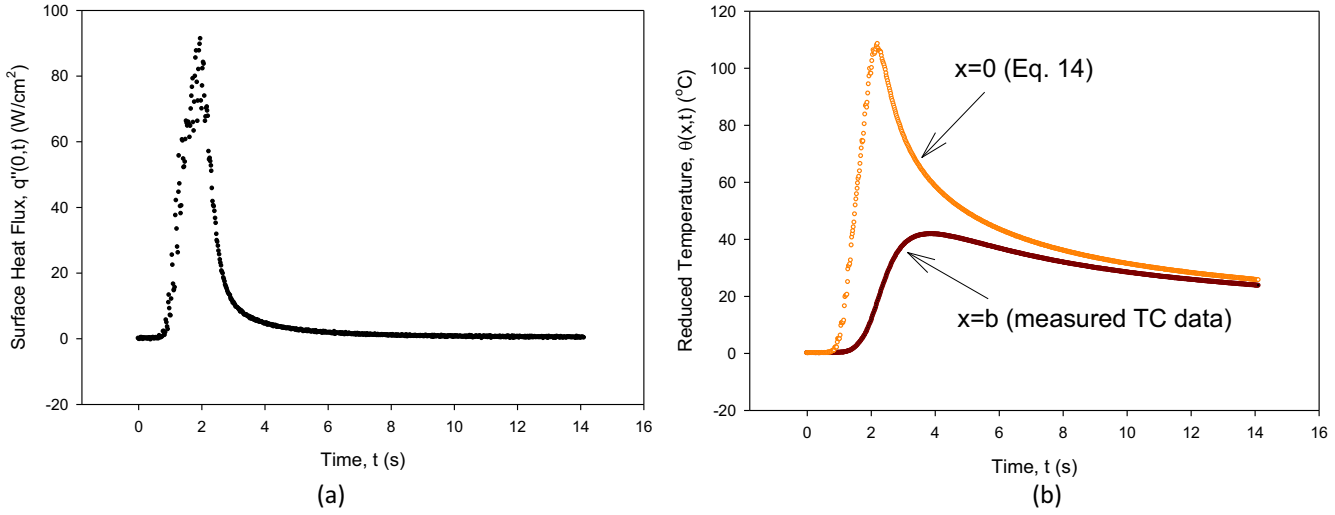

Fig. 10. Higher sampling results (53.3 Hz) for (a) surface heat flux, and (b) indicated reduced temperatures.

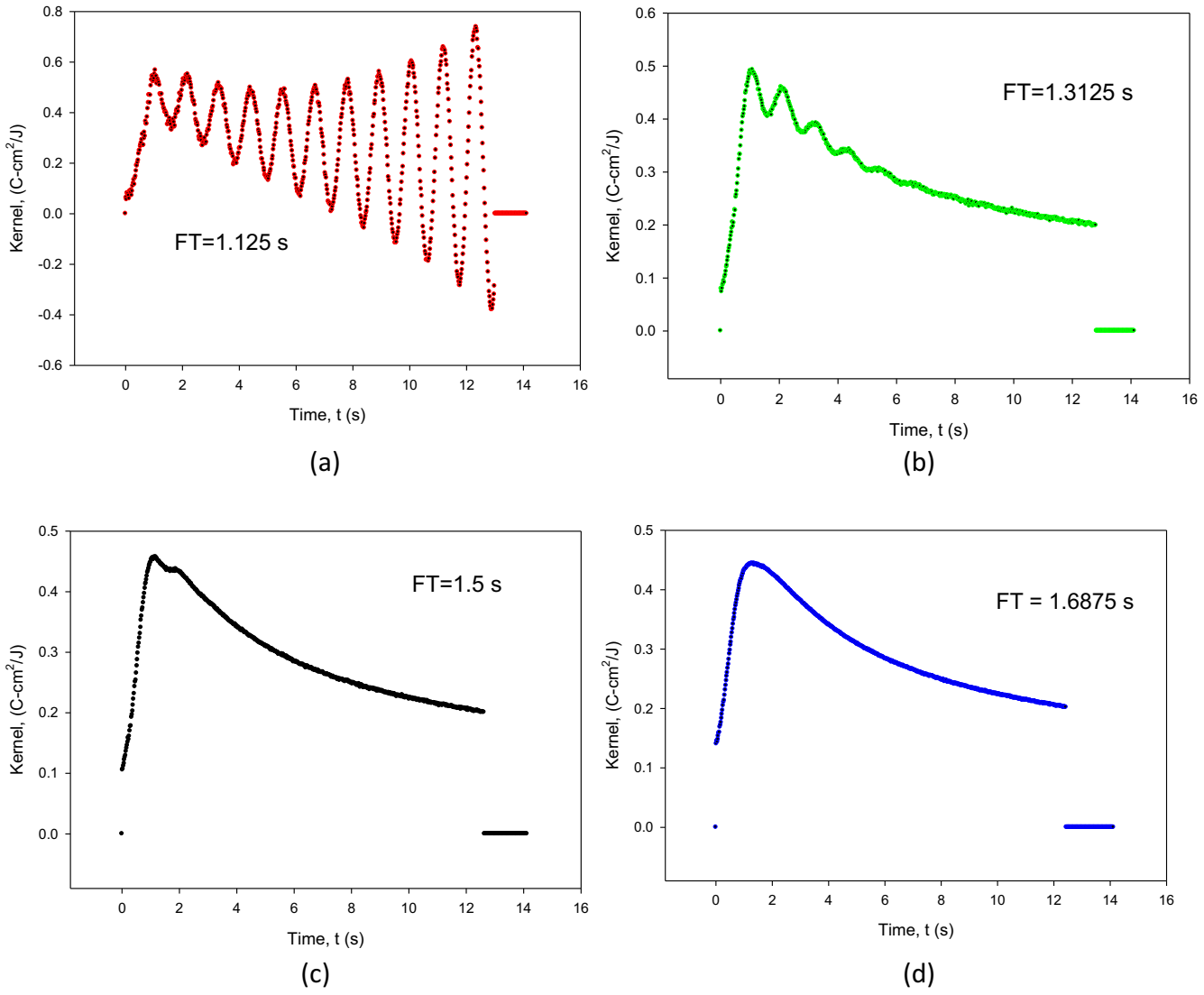

Fig. 11. Transient impulse response kernels, $\tilde{\tilde{K}}_{\bar{\gamma}_{\bar{m}}\bar{N}}(t_i),\ i=1,2,\ldots,\bar{N}-\bar{m}\bar{M}_f,\ \bar{m}=6-9$ using various future-time (FT) parameters: (a) $\bar{\gamma}_{\bar{m}=6}=1.125$ s; (b) $\bar{\gamma}_{\bar{m}=7}=1.3125$ s; (c) $\bar{\gamma}_{\bar{m}=8}=1.5$ s; and, (d) $\bar{\gamma}_{\bar{m}=9}=1.6875$ s when the sampling frequency is 53.3 Hz.

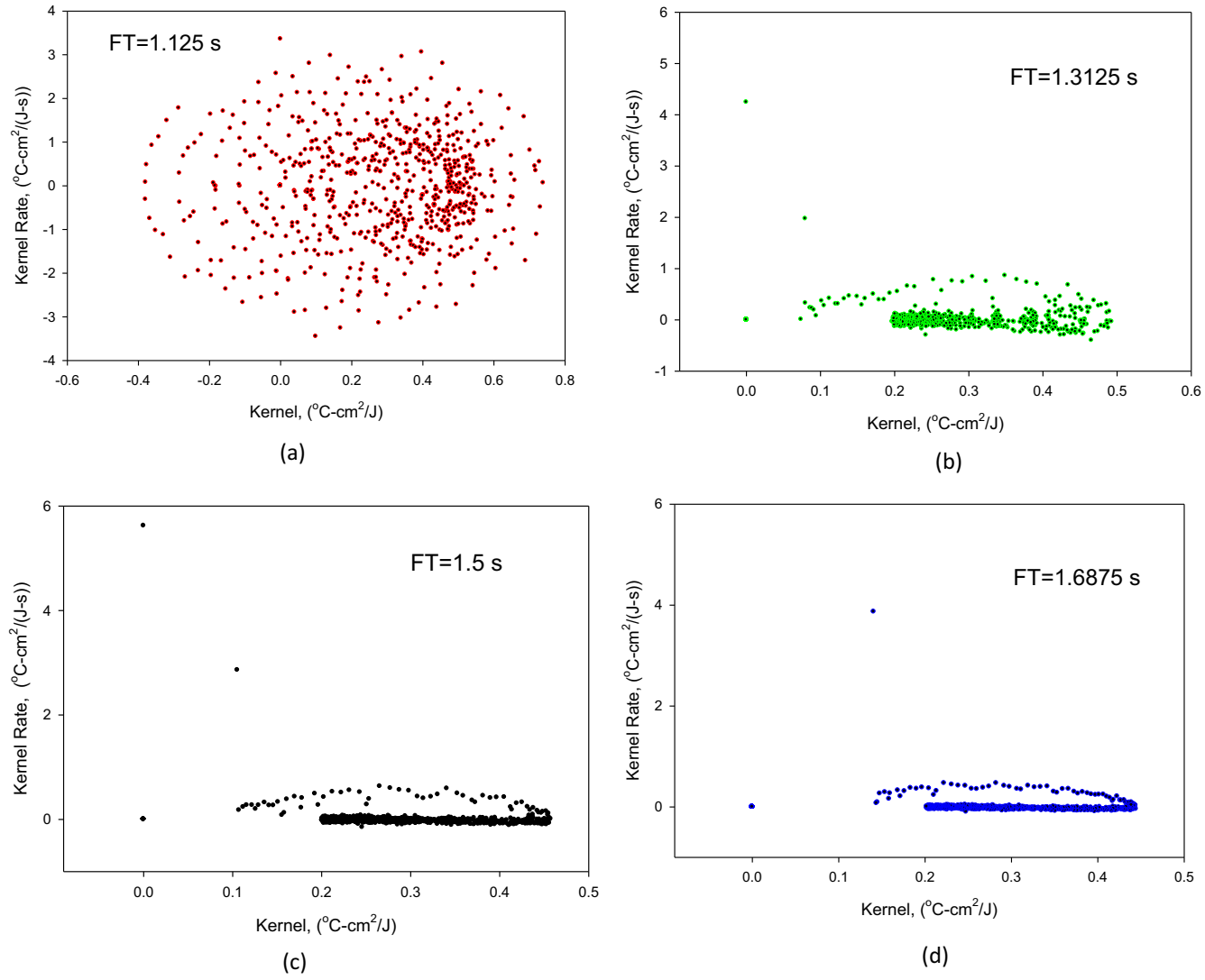

Fig. 12. Transient impulse response kernel phase plane using various future-time (FT) parameters: (a) $\bar{\gamma}_{\bar{m}=6} = 1.125\,\text{s}$; (b) $\bar{\gamma}_{\bar{m}=7} = 1.3125\,\text{s}$; (c) $\bar{\gamma}_{\bar{m}=8} = 1.5\,\text{s}$; and, (d) $\bar{\gamma}_{\bar{m}=9} = 1.6875\,\text{s}$ when the sampling frequency is 53.3 Hz.

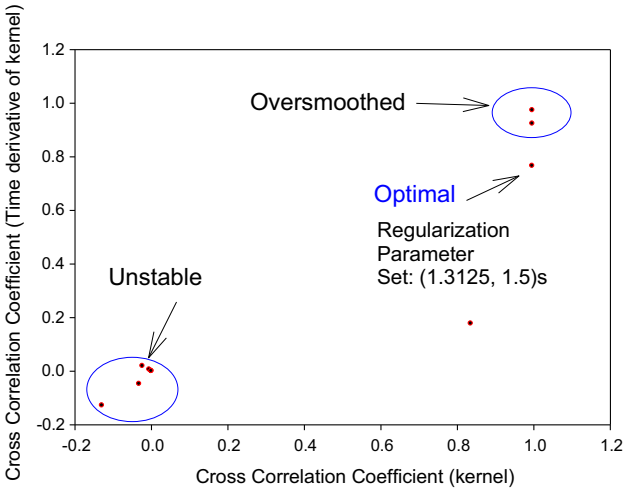

Fig. 13. Cross-correlation phase-plane when the sampling frequency is $f = 53.3$ Hz.

thermocouple merely measures its temperature while in many incidences the true positional temperature is needed as defined by the heat equation. This occurrence is especially noticeable in short- time experimental campaigns where delay and attenuation effect are observed due to the intrusiveness of the probe. As each experiment depends on the choice of thermocouple type, gauge, exposed bead (or enclosed), adhesive or welded, etc. a single "general" metric is difficult to define. However, once $\tilde{\bar{K}}_{\bar{\gamma}_{optimal},\bar{N}}(t_i),\ i = 1,2,\ldots,\bar{N} - \bar{m}\bar{M}_f$ is established, the model kernel function (in this study, Eq. (17c)) should overlay well. If not then extension of the thermocouple model is required.

This preliminary study suggests a procedure for reconstructing an experimentally obtained impulse response function requiring a minimal number of parameters to be determined. This reduction leads to a simple numerical procedure and code. The phase plane demonstrates a quick qualitative process for estimating the optimal regularization parameter by visually removing unstable and over-smoothed predictions. This qualitative viewpoint seeks to indentify the jump condition between instability and a smoothing trend while retaining as much of the signal's higher frequencies

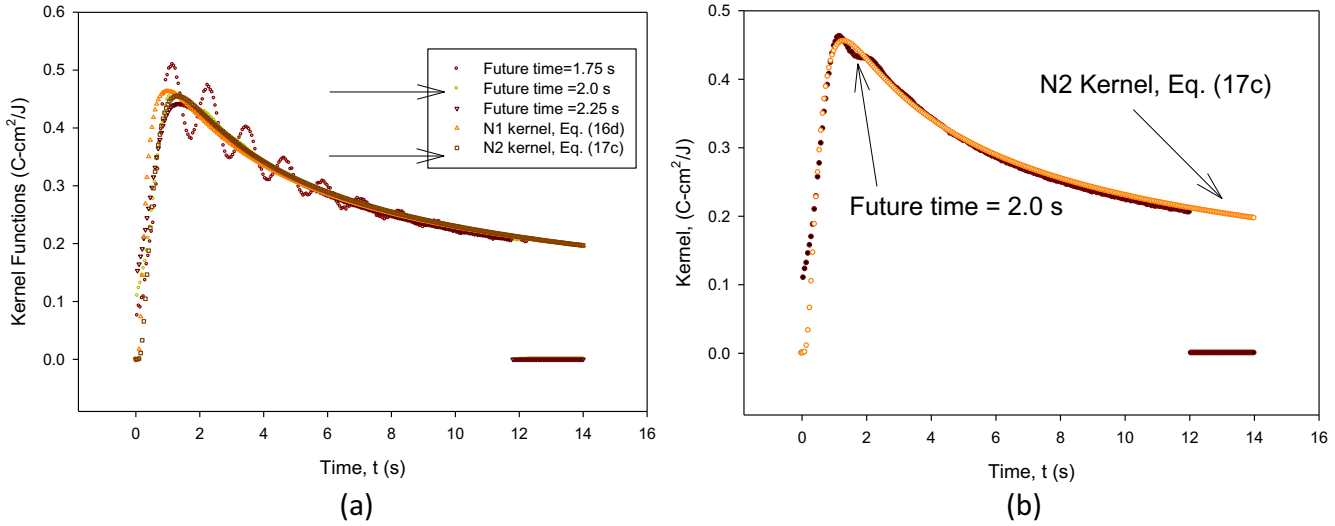

Fig. 14. Predicted impulse response kernel for (a) $\bar{\gamma}_7 = 1.75$ s, $\bar{\gamma}_8 = 2.0$ s, $\bar{\gamma}_9 = 2.25$ s; $N_1(b, t-u; k, \alpha)$ which assumes ideal sensor (no smearing effects); and, $N_2(b, t-u; k, \alpha, \tau)$ which describes the kernel of a first-order thermocouple model based on a 20 Hz sampling frequency; and, (b) comparing $N_2(b, t-u; k, \alpha, \tau)$ to $\bar{\gamma}_8 = 2.0$ s.

as possible. Higher frequencies in the prediction are removed as the regularization parameter, $\bar{\gamma}_{\bar{m}}$ increases; hence, producing a filtering or smoothing action. The cross-correlation coefficient phase plane and analysis represents a metric based calculation that assists in identifying the optimal regularization parameter.

A practical implementation, using the concepts of this paper, involves "thermocouple plugs" as implemented by aerospace and material evaluation applications. Prior to installing the plug into a test article, a campaign would be performed using a known heat flux source on the plug (installed in a temporary plate) to validate the temperature correction (i.e., measured temperature to positional temperature). The plug would then be removed from the test cell and installed into the test article for further studies. Short-time experiments will also greatly benefit as the temperature correction would be established. In short-time experiments, the intrusive nature of the probe can produce observable delay and attenuation effects. If the surface heat flux is desired then Eq. (5b) with

$$\widetilde{\theta}_{tc}(b, t_i) \approx \theta_{tc}(b, t_i) \quad \text{and} \quad \widehat{K}(t_i) \approx \widehat{\widetilde{K}}_{\bar{\gamma}_{optimal}, \bar{N}}(t_i), \; i = 1, 2, ..., \bar{N} - \bar{m}\,\bar{M}_f$$

becomes available. Hence, both the in-depth positional temperature and the surface heat flux are calculable.

Declaration of Competing Interest

The authors declared that there is no conflict of interest.

Acknowledgements

This work was supported by the National Science Foundation [Grant Number: NSF-CBET-1703442].

Appendix A. Supplementary material

Supplementary data to this article can be found online at https://doi.org/10.1016/j.ijheatmasstransfer.2019.05.098.

References

[1] T.E. Diller, in: Advances in Heat Flux Measurements, Academic Press, New York, 1993, pp. 279–368.
[2] F.K. Lu, D.E. Marren, in: Advanced Hypersonic Test Facilities, American Institute of Aeronautics and Astronautics Inc, Reston, VA, 2002, pp. 279–314.
[3] W.J. Cook, E.J. Felderman, Reduction of data from thin-film heat-transfer gages-a concise numerical technique, AIAA J. 4 (3) (1966) 561–562.
[4] F.K. Lu, K.M. Kinnear, Characterization of thin-film heat-flux gauges, J. Thermophys. Heat Transfer 13 (4) (1999) 548–550.
[5] E. Piccini, S.M. Guo, T.V. Jones, The development of a new direct-heat-flux gauge for heat-transfer facilities, Meas. Sci. Technol. 11 (4) (2000) 342–349.
[6] K.A. Woodbury, Effect of thermocouple sensor dynamics on surface heat flux predictions obtained via inverse heat transfer analysis, Int. J. Heat Mass Transf. 33 (12) (1990) 2641–2649.
[7] J.I. Frankel, B.E. Elkins, B.M. Keyhani, Rate-based sensing concepts for heat flux and property estimation; and, transition detection, 16th AIAA/DLR/DGLR International Space Planes and Hypersonic Systems and Technologies Conference, Bremen, Germany, 2009.
[8] T. Blanchat, L. Humphries, W. Gill, Sandia Heat Flux Gauge Thermal Response and Certainty Models, Sandia Report, SAND2000-1111, Albuquerque, NM, 2000.
[9] J.V. Beck, B. Blackwell, C.R. Clair Jr., Inverse Heat Conduction: Ill-Posed Problems, John Wiley & Sons, New York, 1985.
[10] M.N. Ozisik, H.R.B. Orlande, Inverse Heat Transfer: Fundamentals and Applications, Taylor & Francis, New York, 2000.
[11] K. Kurpisz, A. Nowak, Inverse Thermal Problems, Computational Mechanics Publ, Southampton, UK, 1995.
[12] J.I. Frankel, H.C. Chen, K. Mathew, Design-to-validation of a new heat flux source with uncertainty analysis, AIAA J. Thermophys. Heat Transfer 33 (2) (2019) 517–535.
[13] S. Löhle, U. Fuchs, P. Digel, T. Hermann, J.L. Battaglia, Analysing inverse heat conduction problems by the analysis of the system impulse response, Inverse Prob. Sci. Eng. 22 (2) (2014) 297–308.
[14] J.L. Battaglia, O. Cois, L. Puigsegur, A. Oustaloup, Solving an inverse heat conduction problem using a non-integer identified model, Int. J. Heat Mass Transf. 44 (14) (2001) 2671–2680.
[15] J.L. Gardarein, J.L. Battaglia, S. Löhle, Heat flux sensor calibration using noninteger system identification: theory, experiment, and error analysis, Rev. Sci. Instrum. 80 (2) (2009) 025103.
[16] S. Löhle, J.L. Battaglia, P. Jullien, B. van Ootegem, J. Couzi, J.P. Lasserre, Improvement of high heat flux measurement using a null-point calorimeter, J. Spacecraft Rockets 45 (1) (2008) 76–81.
[17] S. Löhle, J.I. Frankel, Physical insight into system identification parameters applied to inverse heat conduction problems, J. Thermophys. Heat Transfer 29 (3) (2015) 467–472.
[18] J.I. Frankel, Regularization of inverse heat conduction by combination of rate sensors analysis and analytic continuation, J. Eng. Math. 57 (2007) 181–198.
[19] M.N. Ozisik, Heat Conduction, Wiley, NY, 1980.
[20] R. Kress, Linear Integral Equations, third ed., Springer-Verlag, New York, 1989.
[21] P. Linz, Analytical and Numerical Methods for Volterra Equations, SIAM, Philadelphia, PA, 1985.
[22] G.M. Wing, A Primer on Integral Equations of the First Kind, SIAM, Philadelphia, PA, 1991.
[23] I. Stakgold, Green's Functions and Boundary Value Problems, Wiley, NY, 1978, Ch. 8.
[24] J.I. Frankel, M. Keyhani, Cross correlation and inverse heat conduction by a calibration method, AIAA J. Thermophys. Heat Transfer 31 (3) (2017) 746–756.

[25] J.I. Frankel, M. Keyhani, Phase-plane and cross-correlation analysis for estimating optimal regularization in inverse heat conduction, J. Thermophys. Heat Transfer 28 (3) (2014) 542–548.
[26] J.I. Frankel, H.C. Chen, M. Keyhani, New step response formulation for inverse heat conduction, AIAA J. Thermophys. Heat Transfer 31 (4) (2017) 989–996.
[27] J.R. Shenefelt, R. Luck, R.P. Taylor, J.T. Berry, Solution to inverse heat conduction problems employing singular value decomposition and model reduction, Int. J. Heat Mass Transfer 45 (2002) 67–74.
[28] F.P. Incropera, D.P. DeWitt, T.L. Bergman, A.S. Lavine, Fundamentals of Heat and Mass Transfer, sixth ed., John Wiley & Sons, New York, 2006.